In-Situ Formed Magnesiophilic Sites Guiding Uniform Deposition for Stable Magnesium Metal Anodes

Gaoliang Yang[‡1], Yuanjian Li[‡1], Chang Zhang[‡2], Jianbiao Wang[1], Yang Bai[1], Carina Yi Jing Lim[1], Man-Fai Ng[3], Zhi Chang[4], Sonal Kumar[1], Zdenek Sofer[5], Wei Liu[2], and Zhi Wei Seh*[1]

1. Institute of Materials Research and Engineering, Agency for Science, Technology and Research (A*STAR), 2 Fusionopolis Way, Innovis, Singapore 138634, Singapore

2. School of Physical Science and Technology, ShanghaiTech University, Shanghai 201210, China

3. Institute of High Performance Computing, Agency for Science, Technology and Research (A*STAR), 1 Fusionopolis Way, Connexis, Singapore 138632, Singapore

4. Department of Materials Physics and Chemistry, School of Materials Science & Engineering, Central South University, Changsha, 410083, Hunan, China

5. Department of Inorganic Chemistry, University of Chemistry and Technology Prague, Technicka´ 5, 166 28 Prague 6, Czech Republic

[‡], These authors contributed equally to this work

*Author to whom correspondence should be addressed.

Email: sehzw@imre.a-star.edu.sg

Abstract:

Owing to its high volumetric capacity and natural abundance, magnesium (Mg) metal has attracted tremendous attention as an ideal anode material for rechargeable Mg batteries. Despite Mg deposition playing an integral role in determining the cycling lifespan, its exact behavior is not clearly understood yet. Herein, for the first time, we introduce a facile approach to build magnesiophilic In/MgIn sites *in-situ* on Mg metal surface using $InCl_3$ electrolyte additive for rechargeable Mg batteries. These magnesiophilic sites can regulate Mg deposition behaviors by homogenizing the distributions of Mg-ion flux and electric field at the electrode-electrolyte interphase, allowing flat and compact Mg deposition to inhibit short-circuiting. The as-designed Mg metal batteries achieve a stable cycling lifespan of 340 h at 1.0 mA cm^{-2} and 1.0 mAh cm^{-2} using Celgard separators, while the full cell coupled with Mo_6S_8 cathode maintains a high capacity retention of 95.5% over 800 cycles at 1 *C*.

Although lithium-ion batteries (LIBs) have prevailed as the dominant technology for energy storage, rising energy demands arising from impending climate change and soaring global population have prompted the search for alternative battery technologies with higher energy densities, enhanced safety and lower costs.[1-4] Moreover, given the relative scarcity of lithium resources, phasing out lithium for more abundant elements has also garnered increasing attention in recent years.[5, 6] Among various post-LIBs technologies, rechargeable magnesium batteries (RMBs) stand out owing to magnesium's (Mg) relative high abundance and high theoretical volumetric capacity of 3833 mAh cm^{-3}.[7, 8] Nevertheless, a myriad of problems still plague Mg anodes and hinder their practical adoption, including surface passivation and non-uniform Mg deposition.[8-11]

Tremendous efforts have since been devoted to address the passivation issue of Mg anodes, such as designing novel electrolytes[12-14] or introducing various anions/chelants to regulate the coordination structure.[15, 16] However, problems surrounding Mg deposition behaviors are often neglected, despite playing a key role in the performance of Mg anodes.[17, 18] Since the first Mg battery prototype in 2000,[19] Mg metal anodes were initially thought to be non-dendritic due to homogeneous diffusion of Mg^{2+} under moderate working conditions.[20, 21] However, with gradually deepened understanding of the anode-electrolyte interphase, it was found that Mg deposition behaviors depend on the interplay between deposition rate, surface diffusion rate and diffusion barrier.[18, 22] Uneven or dendritic Mg deposition occurs when the rate of electrochemical reaction

surpasses the self-diffusion rate, which is commonly observed under high current densities and poor surface properties.[22-24] In addition, concentration gradients as well as electric fields at the electrode-electrolyte interphase are also critical factors dictating the deposition morphology.[17]

In this study, we demonstrate a facile approach to build magnesiophilic sites *in-situ* on the Mg metal surface using InCl$_3$ electrolyte additive in RMBs for the first time. Such magnesiophilic sites serve to regulate the deposition behaviors with flat and uniform Mg deposition morphology, while also enabling fast electrochemical reaction kinetics. As revealed by COMSOL simulations, owing to the uniquely compact deposition morphology, the Mg^{2+} flux is homogenized and the local current density is reduced at the anode-electrolyte interphase, resulting in stable Mg metal anodes.

Results and Discussion

Indium (In) presents relatively inert and nonreactive properties with most solvents or electrolyte salts,[25, 26] as well as good affinity to Mg.[27] Additionally, due to the difference in electronegativity, In^{3+} can also react with Mg metal *via* ion exchange reaction to form In metal and Mg ions.[28, 29] Owing to the mutually enhanced solubility of magnesium triflate (Mg(OTf)$_2$) and metal chlorides combination in 1,2-dimethoxyethane (DME) solvent,[30] InCl$_3$ salt was selected as the additive for electrolyte modification and electrolytes with varying ratios of Mg(OTf)$_2$ and InCl$_3$ were prepared in DME. Interestingly, clear and stable electrolyte solutions are obtained when the molar ratio of Mg(OTf)$_2$ to InCl$_3$ is greater than 1 (Figure S1a-b). Subsequently, Mg//Al asymmetric cells were assembled to evaluate the reversibility of Mg plating/stripping with the as-prepared electrolytes. Due to serious surface passivation, the Mg//Al cell using pure Mg(OTf)$_2$ electrolyte is only lasted

for 60 cycles, with a low average Coulombic efficiency (CE) of 71.6% and a high voltage polarization at 0.05 mA cm^{-2} and 0.05 mAh cm^{-2} (Figure S2). In contrast, the modified electrolytes with different Mg(OTf)$_2$-InCl$_3$ combinations demonstrate significantly enhanced reversibility for Mg plating/stripping. As depicted in Figure S3, the 0.4 M Mg(OTf)$_2$ + 0.2 M InCl$_3$ electrolyte achieves a long cycling lifespan of 250 cycles, with a high average CE of 98.7% and a low voltage polarization of ~0.15 V, which is the best amongst all fully soluble electrolytes with InCl$_3$ additive. Hereafter, all the characterizations are based on the 0.4 M Mg(OTf)$_2$ + 0.2 M InCl$_3$ electrolyte (abbreviated as Mg(OTf)$_2$ + InCl$_3$), unless stated otherwise.

The optical images (insets in Figure 1a-1b) reveal that the color of Mg anode changes from silver to grey after resting in the coin cell for 3 h with Mg(OTf)$_2$ + InCl$_3$ electrolyte. The corresponding scanning electron microscopy (SEM) images (Figure 1a-1b; Figure S4a-S4c) show that the surface of Mg metal with In modification is covered by a large number of granular-like nanoparticles. Energy-dispersive X-ray spectroscopy (EDS) mapping images in Figure S4d verify the uniform distribution of In across the entire surface of modified Mg metal. To further investigate the detailed composition of the *in-situ* formed granules on Mg metal, X-ray diffraction (XRD) and X-ray photoelectron spectroscopy (XPS) measurements were employed. As shown in Figure 1c, the characteristic peaks of In metal are detected from the modified Mg metal. Intriguingly, in addition to metallic In and its oxide (In$_2$O$_3$), the Mg-In alloy peak (~441.7 eV) is also observed from the In *3d* spectrum (Figure S5),[31, 32] and the relative ratio of the Mg-In alloy to In and In$_2$O$_3$ increases after 5 min of Ar etching (Figure S5b). To confirm the detailed structure of Mg-In alloy in modified Mg metal, the bare Mg metal was immersed in Mg(OTf)$_2$ + InCl$_3$ electrolyte for a longer duration

to allow for greater degree of reaction.[33] The corresponding XRD pattern (Figure S6) further verifies the existence of Mg-In alloy as evidenced by its characteristic peak at around 27.8°, corresponding to the (101) plane of MgIn phase. To reveal greater insights on Mg affinity, density functional theory (DFT) calculation was utilized to compare the adsorption energy (E_{ad}) of Mg atoms onto different crystal planes (obtained from the XRD patterns in Figure S6). Impressively, the E_{ad} of Mg atoms on In (101), MgIn (001) and MgIn (101) are −1.36 eV, −1.56 eV and −0.81 eV, respectively, which are more negative than that of Mg (002) (−0.75 eV; Figure 1d). This highlights the magnesiophilic nature of the In/MgIn sites with lower energy barriers of Mg nucleation to promote uniform Mg deposition at different growth stages (Figure 1e).[34] In fact, at 0.5 mA cm^{-2} and 0.5 mAh cm^{-2}, Mg(OTf)$_2$ + InCl$_3$ electrolyte showed flat and compact Mg deposits, while pure Mg(OTf)$_2$ produced nonuniform Mg spheres and rods (Figure 1f-h and Figure S7-S10).
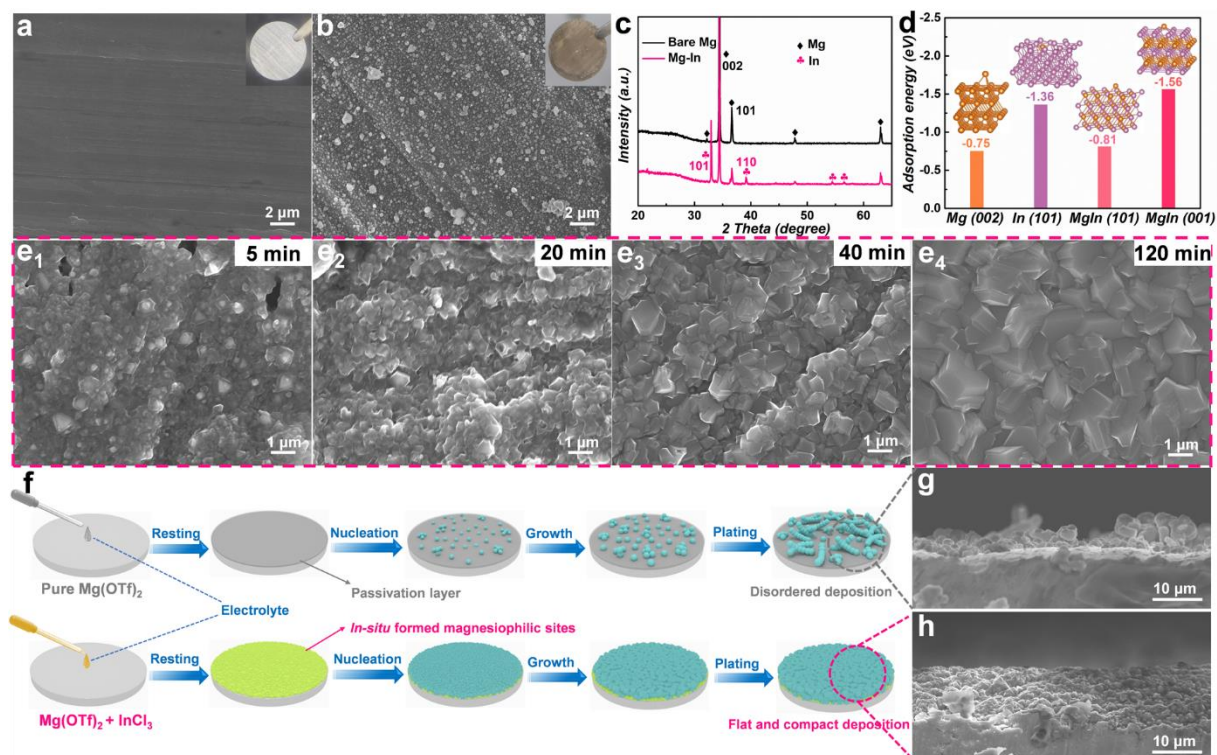
Figure 1. Optical images and corresponding SEM images of a) bare Mg and b) Mg electrode reacted with $Mg(OTf)_2$ + $InCl_3$ electrolyte. c) XRD patterns of Mg electrodes before and after reacting with $Mg(OTf)_2$ + $InCl_3$ electrolyte. d) Calculated adsorption energies of Mg atoms onto different crystal facets. e) SEM images of Mg deposit evolution at different growth stages at a current density of 0.5 mA cm^{-2}. f) Schematic illustration of Mg deposition morphology evolution on the Mg anode in pure $Mg(OTf)_2$ and $Mg(OTf)_2$ + $InCl_3$ electrolytes during the plating process. Cross-sectional SEM images of Mg deposits in different electrolytes of g) pure $Mg(OTf)_2$ and h) $Mg(OTf)_2$ + $InCl_3$ at 0.5 mA cm^{-2} and 0.5 mAh cm^{-2}.

To explore the evolution of Mg deposition morphology with varied current densities, a series of Mg plating experiments are conducted. According to the measurement of critical current density in Figure S11,[35] the symmetric cell with pure $Mg(OTf)_2$ electrolyte is only viable under current

densities below 0.5 mA cm^{-2}. Therefore, the evolution of deposition morphology in pure Mg(OTf)$_2$ was conducted from 0.05 to 0.5 mA cm^{-2}. As displayed in Figure 2a, Mg deposits form with particulate morphology at a low current density of 0.05 mA cm^{-2}. As the current densities increase to 0.1 and 0.25 mA cm^{-2}, the Mg deposits gradually coalesce into stacked spheres with non-uniform distribution. When the current density increases to 0.5 mA cm^{-2}, the stacked spheres further grow and merge together, finally forming Mg rods (Figure 2a$_4$ and Figure S12). If such Mg deposits continuously grow vertically (marked with red circles in Figure S9), they will rapidly perforate through the separator, resulting in short-circuiting failure.[17] This is consistent with the critical-current-density result in Figure S11, indicating that pure Mg(OTf)$_2$ electrolyte is not feasible under high current densities due to the short circuit event. On the other hand, Mg deposition morphology in Mg(OTf)$_2$ + InCl$_3$ electrolyte exhibits a consistently flat and uniform appearance under different working conditions (from 0.5 to 3.0 mA cm^{-2}), which is credited to the regulative effects of the *in-situ* formed magnesiophilic In/MgIn sites on Mg deposition behaviors (Figure 2b).

From literature reports, MgCl$_2$ is the most common additive for conventional electrolytes in RMBs, which may alleviate passivation issues of Mg electrodes and alter the deposition morphology.[30, 36-38] In order emphasize the effects of *in-situ* formed In/MgIn magnesiophilic sites, InCl$_3$ was replaced by MgCl$_2$ in the electrolyte and the relevant Mg deposition morphology was investigated under the same working condition. As shown in Figure 2c, at a current density of 0.5 mA cm^{-2}, the deposited Mg displays block-shaped morphology with some voids across the deposition layer, indicative of rough deposition in Mg(OTf)$_2$ + MgCl$_2$ electrolyte. When the current density is increased to 1.0 mA cm^{-2}, flake-like Mg deposits start to appear. As the current density is further increased, flake-

like Mg deposits become thinner and sharper, before finally covering the whole electrode surface with sharp deposits when the current density reaches 3.0 mA cm^{-2}. With the continuous growth of these sharp Mg dendrites during cycling, the risk of internal short-circuiting may be aggravated (Figure S13).[30]
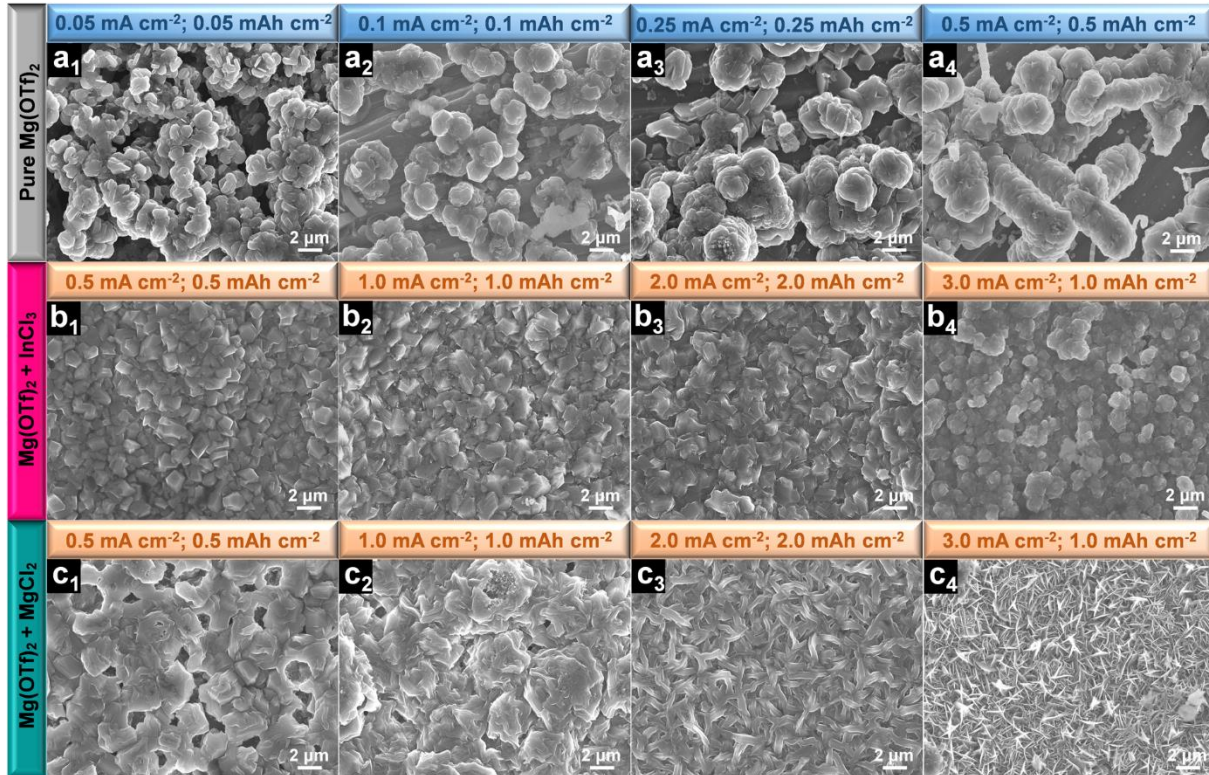

Figure 2. The morphology evolution of Mg deposition under different current densities and areal capacities in different electrolytes of a) pure Mg(OTf)$_2$, b) Mg(OTf)$_2$ + InCl$_3$ and c) Mg(OTf)$_2$ + MgCl$_2$.

In addition, we also probe the influence of the InCl$_3$ additive on the electrochemical reaction kinetics. Generally, in the voltage-time curve of Mg plating, the initial peak voltage represents the nucleation overpotential (μ_n), which is related to the energy barrier of the heterogeneous nucleation process.[39, 40] As reflected in Figure 3a, at a current density of 0.5 mA cm^{-2}, a low μ_n of 0.23 V is

achieved in $Mg(OTf)_2$ + $InCl_3$ electrolyte. This value is much smaller than that of $Mg(OTf)_2$ + $MgCl_2$ (0.98 V) and pure $Mg(OTf)_2$ (1.60 V), verifying the reduced energy barrier for Mg nucleation with In/MgIn sites, which are consistent with the DFT calculation results. As Mg deposition continues, the overpotential would decrease and reach a stable plateau value (μ_p). Strikingly, the μ_p in $Mg(OTf)_2$ + $InCl_3$ is a mere 0.18 V, while that in $Mg(OTf)_2$ + $MgCl_2$ and pure $Mg(OTf)_2$ are 0.42 V and 1.47 V, respectively. In general, a lower overpotential is indicative of faster charge and mass transfer processes.[41] This enhanced kinetics is confirmed by electrochemical impedance spectroscopy (EIS) results in Figure S14 and Table S1, where the charge transfer resistance (R_{ct}) values of Mg//Mg symmetric cells are extracted by fitting the EIS spectra with the equivalent circuit (inset in Figure S14a). The R_{ct} values of the cells with $Mg(OTf)_2$ + $MgCl_2$ and pure $Mg(OTf)_2$ are 281.5 kΩ and 160.9 kΩ, respectively. In contrast, a significantly decreased R_{ct} of 2.223 kΩ is observed with $Mg(OTf)_2$ + $InCl_3$ electrolyte, indicating more efficient charge transfer processes which allows for faster deposition kinetics.[42] The kinetics of Mg deposition could also be quantitatively evaluated from the activation energy (E_a) derived through the Arrhenius equation.[43] Figure S15 displays Nyquist plots of Mg//Mg symmetric cells at different temperatures, from which the R_{ct} values (Table S2) are similarly obtained. The E_a values are then determined from slopes of the linear fits of $\ln(1/R_{ct})$ against 1000/T, where $Mg(OTf)_2$ + $InCl_3$ exhibits the lowest E_a of 21.07 kJ mol^{-1} (Figure 3b). Additionally, the exchange current densities (j_{ex}), derived from the Tafel plots, are compared to reflect the Mg plating/stripping kinetics.[44] As shown in Figure S16, the j_{ex} in $Mg(OTf)_2$ + $InCl_3$ (1.04×10^{-2} mA cm^{-2}) is substantially higher than that of pure $Mg(OTf)_2$ (6.03×10^{-5} mA cm^{-2}) and $Mg(OTf)_2$ + $MgCl_2$ (2.12×10^{-4} mA cm^{-2}),

reinforcing the role of the InCl$_3$ additive in facilitating charge transfer and boosting electrochemical reaction kinetics.[43]

To further validate the regulation effects on deposition behaviors and reaction kinetics, the electrochemical performance in different electrolytes is evaluated using Mg//Mg symmetric cells at 0.5 mA cm^{-2} and 0.5 mAh cm^{-2}. As expected, owing to severe passivation effects and uneven Mg deposition, the symmetric cell with pure Mg(OTf)$_2$ is short-circuited after only 1 cycle (Figure 3c and inset). Even under the mild working condition of 0.05 mA cm^{-2} and 0.05 mAh cm^{-2}, the pure Mg(OTf)$_2$ still displays poor cycling performance with large overpotentials (Figure S17). With the addition of MgCl$_2$, although the cycling lifespan is extended to ~400 h, a sudden short circuit occurs at the 200th cycle as reflected by the inset in Figure 3c. In contrast, the cell with Mg(OTf)$_2$ + InCl$_3$ electrolyte achieves a stable cycling for 600 h and maintains a small polarization voltage of ~0.15 V over 300 cycles. When the working condition is increased to 1.0 mA cm^{-2} and 1.0 mAh cm^{-2} (Figure 3d), the lifespan of the cell using Mg(OTf)$_2$ + MgCl$_2$ is shortened to 130 h (suffering from short circuit at the 65th cycle), with a large overpotential of ~0.30 V. In comparison, a much longer cycling lifespan of 340 h, with a much lower overpotential of ~0.20 V is delivered by the cell with Mg(OTf)$_2$ + InCl$_3$ electrolyte. With future industrial application in mind, Celgard separators (25 μm thick, 2 layers) were primarily used in this work, as opposed to thicker glass fiber separators (~300 μm). Even with Celgard separators, the performance with the Mg(OTf)$_2$ + InCl$_3$ electrolyte is comparable with some reported results using glass fiber separators (Table S3 and Figure S18).

The rate capabilities of symmetric cells were further compared between the different electrolytes at a fixed capacity of 0.5 mAh cm^{-2}. As shown in Figure 3e, when the current density is increased from 0.5 to 4 mA cm^{-2}, Mg(OTf)$_2$ + InCl$_3$ consistently presents substantially lower voltage hysteresis than Mg(OTf)$_2$ + MgCl$_2$. Moreover, the overpotential can be recovered to ~0.15 V when the current density is decreased from 4 to 0.5 mA cm^{-2}, suggesting a stellar reversibility with the Mg(OTf)$_2$ + InCl$_3$ electrolyte. For Mg(OTf)$_2$ + MgCl$_2$, however, a sudden voltage plunge is observed when the current density reaches 3 mA cm^{-2} (inset in Figure 3e). This phenomenon may be related to the deposition morphology as previously observed in Figure 2c, which displays a significant change in the shape of Mg deposits to a sharp flake-like structure at 3 mA cm^{-2}. Thus, the above electrochemical performance in different electrolytes emphasizes the importance of understanding deposition behaviors in Mg metal batteries, especially under high current densities. Furthermore, the (elelctro)chemical stability of as-designed metallic sites during the cycling is also reflected by the SEM images and corresponding EDS mappings of the Mg anode reacted with InCl$_3$ additive (Figure S19), which shows that the morphology and structure of the *in-situ* formed In/MgIn sites are maintained after cycling.
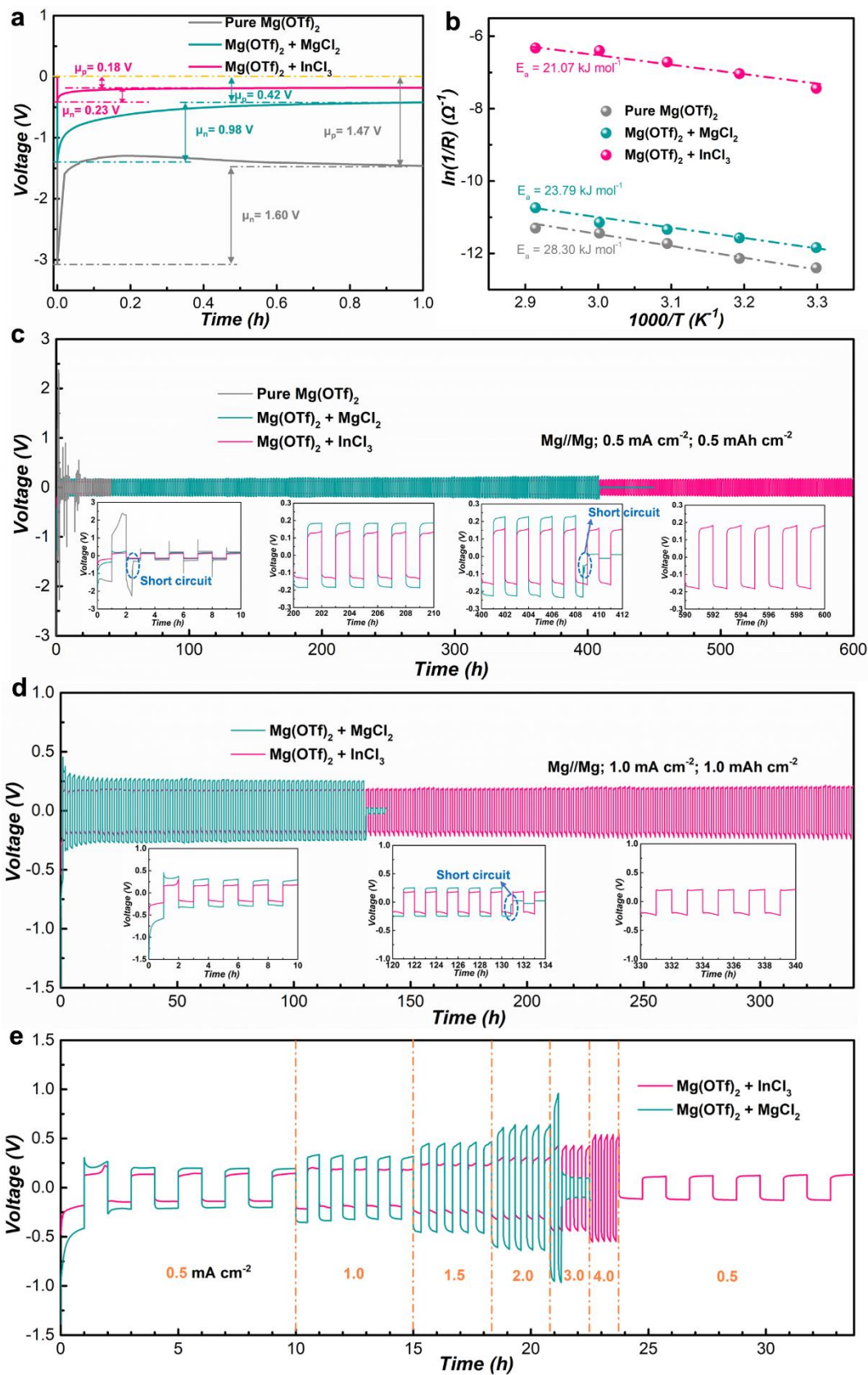
Figure 3. a) Initial discharging voltage profiles of Mg deposition at a current density of 0.5 mA cm^{-2} and b) calculated E_a using Arrhenius equation in different electrolyte of pure Mg(OTf)$_2$, Mg(OTf)$_2$ + MgCl$_2$ and Mg(OTf)$_2$ + InCl$_3$. Galvanostatic cycling performance of Mg//Mg symmetric cells at c) 0.5 mA cm^{-2} and 0.5 mAh cm^{-2}; d) 1.0 mA cm^{-2} and 1.0 mAh cm^{-2}. The inserts in Figure 3c and Figure 3d are expanded voltage profiles of Mg//Mg symmetric cells at different stages during cycling. e) The rate capability of Mg//Mg symmetric cells at various current densities from 0.5 mA cm^{-2} to 4 mA cm^{-2} with a fixed capacity of 0.5 mAh cm^{-2}.

To understand the dynamic behavior of Mg electrode during deposition in different electrolytes, finite element method (FEM) was conducted to investigate the Mg^{2+} concentration and electrical field distributions at the electrode-electrolyte interphase by COMSOL simulation (Figure S20-S21).[40] 2D geometric models (Figure S22 and Figure S24) were built based on the SEM results in Figure 2. As depicted in Figure 4a and Figure S23a, at a current density of 0.5 mA cm^{-2}, due to the protruding Mg deposits in pure Mg(OTf)$_2$, the Mg-ion flux and electric field tend to concentrate around the sharp edges,[34] indicating that further Mg deposition will preferentially occur on the protuberance sites, ultimately leading to short circuiting with the continuous growth of Mg protrusions (consistent with the cycling performance of pure Mg(OTf)$_2$ in Figure 3c). Owing to the relatively flat deposition morphology in Mg(OTf)$_2$ + MgCl$_2$ and Mg(OTf)$_2$ + InCl$_3$, the ion concentration and electric field distributions are relatively homogenized (Figure 4b-4c; Figure S23b-S23c), which likely enabled the cells with these two electrolytes to cycle normally at 0.5 mA cm^{-2} (Figure 3c). When the current density is increased to 3.0 mA cm^{-2}, the Mg deposits in Mg(OTf)$_2$ + MgCl$_2$ would transform to sharp flake-like morphology (Figure 2c$_4$). Such flake-like

morphology possesses the similar geometric effects as observed with the dendritic structure.[30] Consequently, serious tip effects can be found with distorted distributions of ion concentration and formation of "hot spots" for local electric field (Figure S25a; Figure 4d),[45] leading to the fast short-circuiting failure at 3.0 mA cm^{-2} (Figure 3e). In contrast, due to the consistently flat deposition morphology in Mg(OTf)$_2$ + InCl$_3$, uniform distributions of Mg^{2+} flux and electric field are found across the whole electrode-electrolyte interphase (Figure S25b; Figure 4e), thus minimizing the short-circuiting risk under high current densities and resulting in excellent rate capability.
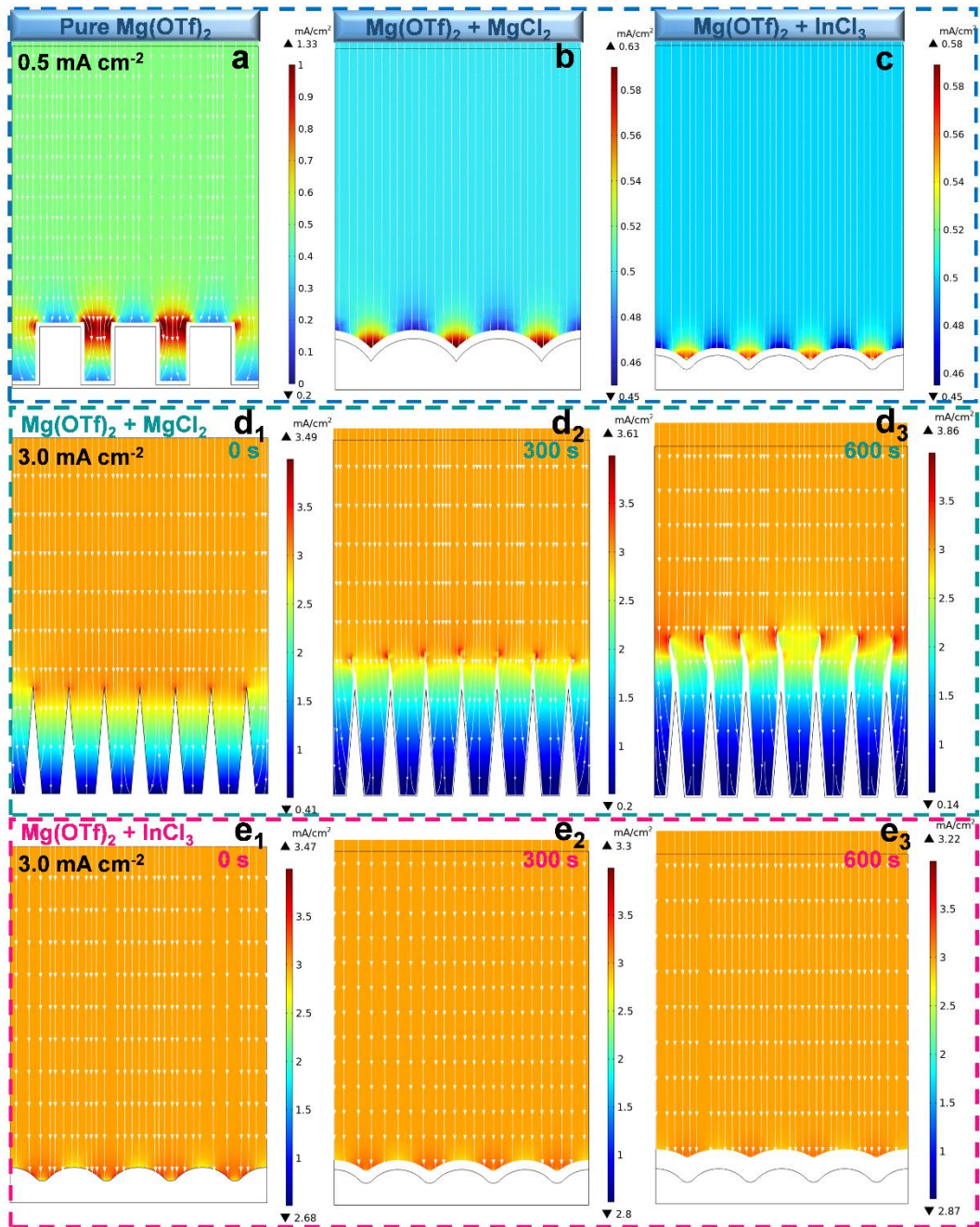
Figure 4. COMSOL simulation regarding the influence of different deposition morphology on the electrical field distribution: Simulated results in different electrolytes of a) pure $Mg(OTf)_2$, b) $Mg(OTf)_2 + MgCl_2$ and c) $Mg(OTf)_2 + InCl_3$ under a low current density of 0.5 mA cm^{-2}. The gradual evolution of electrical field distribution with selected simulation time from 0 s to 600 s in different electrolytes of d) $Mg(OTf)_2 + MgCl_2$ and e) $Mg(OTf)_2 + InCl_3$ under a high current density

of 3.0 mA cm^{-2}.

To evaluate potential application of the modified electrolyte in RMBs, full cells were assembled using Mg metal as anode and Mo$_6$S$_8$ with a Chevrel phase (Figure S26) as cathode. Due to severe passivation effects between Mg electrode and pure Mg(OTf)$_2$ electrolyte, the insertion/extraction reactions for Mg ions are unable to occur in the Mg//Mo$_6$S$_8$ full cell with pure Mg(OTf)$_2$, as indicated by cyclic voltammetry (CV) and charging/discharging curves in Figure S27. In contrast, the CV curves of Mg(OTf)$_2$ + MgCl$_2$ and Mg(OTf)$_2$ + InCl$_3$ both display similar redox peaks (Figure 5a), corresponding to reversible insertion/extraction behaviors of Mg ions from Mo$_6$S$_8$ cathodes.[12] A smaller voltage polarization of Mg(OTf)$_2$ + InCl$_3$, compared with Mg(OTf)$_2$ + MgCl$_2$, is evident in Figure 5a, indicating fast reaction kinetics enabled by InCl$_3$ additives.[46] Figure 5b-5c illustrate the cycling performance of Mg//Mo$_6$S$_8$ cells with Mg(OTf)$_2$ + InCl$_3$ electrolyte and corresponding charging/discharging curves between 0.2 and 2.2 V from 1st to 100th cycle at 0.1 C, respectively. The cell maintains a considerable capacity of 80.2 mAh g^{-1} with a capacity retention of 96.0% over 100 cycles, signifying excellent stability and high compatibility with the Mo$_6$S$_8$ cathode. In addition, the rate performance of full cells with different electrolytes is compared in Figure 5d, in which the cell with Mg(OTf)$_2$ + InCl$_3$ electrolyte achieves much higher capacities at various current densities. Specifically, the Mg//Mo$_6$S$_8$ cells present stable discharging capacities of 37.1 mAh g^{-1} at the corresponding current density of 5 C with the presence of InCl$_3$ additive, while a low capacity of 23.3 mAh g^{-1} is delivered for Mg(OTf)$_2$ + MgCl$_2$. Additionally, Mg(OTf)$_2$ + InCl$_3$ showed enhanced capacity retention upon reverting back from 5 C to 0.1 C (Figure 5d), as well as smaller voltage polarization with increasing current densities (Figure S28). Long-term cycling

performance of the two full cells was further compared at 1 C (Figure 5e). Impressively, the

Mg//Mo$_6$S$_8$ cell with Mg(OTf)$_2$ + InCl$_3$ delivers a reversible capacity of 51.1 mA h g^{-1} after 800

cycles (with an excellent capacity retention of 95.5%), while the control cell with MgCl$_2$ additive

only retains a scant capacity of 29.8 mA h g^{-1} (with a low capacity retention of 76.8%). Moreover,

the corresponding charging/discharging curves demonstrate significantly reduced voltage

polarization with the InCl$_3$ additives (Figure S29), congruent with the CV results. The novel

findings in this work provide insights on the importance of regulating Mg deposition behaviors for

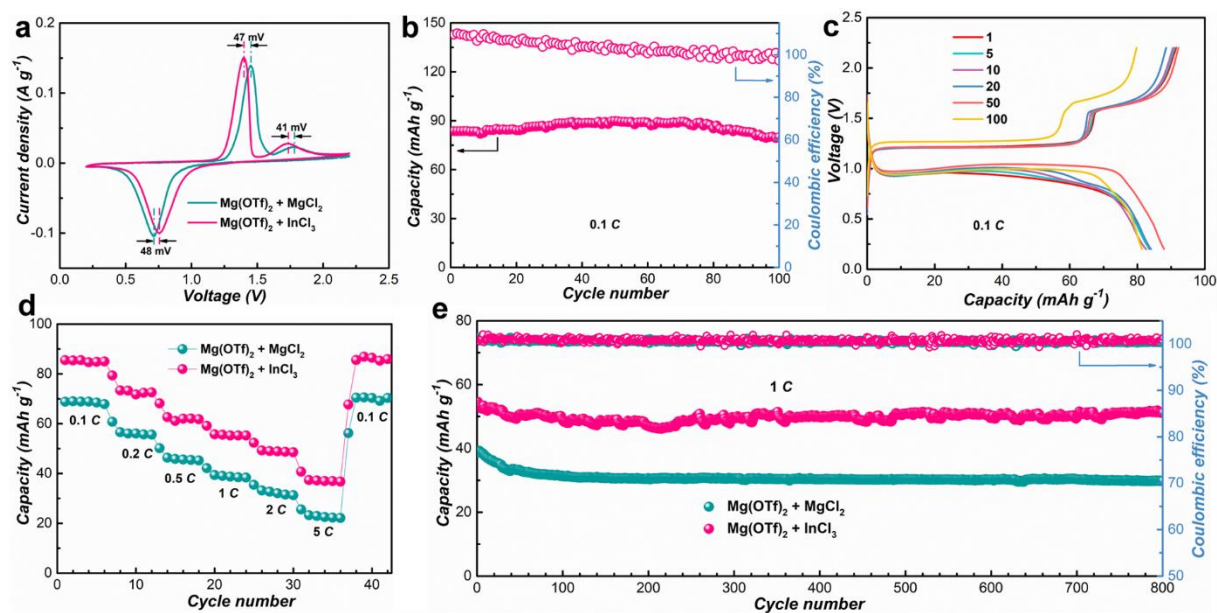high-performance RMBs, which may be applied to other metal anode batteries in the future.

Figure 5. Electrochemical performance of Mg//Mo$_6$S$_8$ full cells in different electrolytes. a) Cyclic

voltammograms with a scan rate of 0.1 mV s^{-1}. b) Cycling performance at 0.1 C over 100 cycles

and c) corresponding charging/discharging curves with a voltage range of 0.2-2.2 V (vs. Mg/Mg^{2+})

in Mg(OTf)$_2$ + InCl$_3$. d) Rate performance at various current densities from 0.1 C to 5 C (1 C = 129

mA g^{-1}). e) Long-term cycling performance at 1 C for 800 cycles.

ASSOCIATED CONTENT

Supporting Information.

The Supporting information provides the experimental details and additional characterizations.

Author Contributions

G. Y. and Z. W. S. conceived the idea. G. Y. prepared the manuscript. G. Y. and Y. L. performed the experiments. C. Z. and W. L. performed the COMSOL simulations. J. W. and Y. B. conducted the XRD characterization. C. Y. J. L. and Z. W. S. revised the manuscript. M.-F. N. carried out the DFT calculations. G. Y., Y. L. and Z. C. conducted the data analysis. S. K. conducted the EDS elemental mapping. Z. S. provided the Mo_6S_8 cathode materials. Z. W. S. supervised the project. All authors discussed the results and commented on the manuscript.

Notes

The authors declare no competing financial interest.

References

1. Zhang, J. G.; Xu, W.; Xiao, J.; Cao, X.; Liu, J. Lithium Metal Anodes with Nonaqueous Electrolytes. *Chem. Rev.* **2020**, *120*, 13312-13348.

2. Eng, A. Y. S.; Soni, C. B.; Lum, Y.; Khoo, E.; Yao, Z.; Vineeth, S. K.; Kumar, V.; Lu, J.; Johnson, C. S.; Wolverton, C.; Seh, Z. W. Theory-guided experimental design in battery materials research. *Sci. Adv.* **2022**, *8*, eabm2422.

3. Lin, D.; Liu, Y.; Cui, Y. Reviving the lithium metal anode for high-energy batteries. *Nat. Nanotechnol.* **2017**, *12*, 194-206.

4. Zhang, X.; Yang, Y.; Zhou, Z. Towards practical lithium-metal anodes. *Chem. Soc. Rev.* **2020**, *49*, 3040-3071.

5. Liang, Y.; Dong, H.; Aurbach, D.; Yao, Y. Current status and future directions of multivalent metal-ion batteries. *Nat. Energy* **2020**, *5*, 646-656.

6. Liu, F.; Wang, T.; Liu, X.; Fan, L. Z. Challenges and Recent Progress on Key Materials for Rechargeable Magnesium Batteries. *Adv. Energy Mater.* **2020**, *11*, 2000787.

7. Muldoon, J.; Bucur, C. B.; Gregory, T. Quest for nonaqueous multivalent secondary batteries: magnesium and beyond. *Chem. Rev.* **2014**, *114*, 11683-720.

8. Liang, Z.; Ban, C. Strategies to Enable Reversible Magnesium Electrochemistry: From Electrolytes to Artificial Solid–Electrolyte Interphases. *Angew. Chem. Int. Ed.* **2021**, *60*, 11036-11047.

9. Sun, Y.; Ai, F.; Lu, Y. C. Electrolyte and Interphase Design for Magnesium Anode: Major Challenges and Perspectives. *Small* **2022**, e2200009.

10. Zhao, W.; Pan, Z.; Zhang, Y.; Liu, Y.; Dou, H.; Shi, Y.; Zuo, Z.; Zhang, B.; Chen, J.; Zhao, X.; Yang, X. Tailoring Coordination in Conventional Ether-Based Electrolytes for Reversible Magnesium-Metal Anodes. *Angew. Chem. Int. Ed.* **2022**, *61*, e202205187.

11. Song, Z.; Zhang, Z.; Du, A.; Dong, S.; Li, G.; Cui, G. Uniform Magnesium Electrodeposition via Synergistic Coupling of Current Homogenization, Geometric Confinement, and Chemisorption Effect. *Adv. Mater.* **2021**, *33*, e2100224.

12. Mizrahi, O.; Amir, N.; Pollak, E.; Chusid, O.; Marks, V.; Gottlieb, H.; Larush, L.; Zinigrad, E.; Aurbach, D. Electrolyte Solutions with a Wide Electrochemical Window for Rechargeable Magnesium Batteries. *J. Electrochem. Soc.* **2008**, *155*, A103.

13. Luo, J.; Bi, Y.; Zhang, L.; Zhang, X.; Liu, T. L. A Stable, Non-Corrosive Perfluorinated Pinacolatoborate Mg Electrolyte for Rechargeable Mg Batteries. *Angew. Chem. Int. Ed.* **2019**, *58*, 6967-6971.

14. Horia, R.; Nguyen, D.-T.; Eng, A. Y. S.; Seh, Z. W. Using a Chloride-Free Magnesium Battery Electrolyte to Form a Robust Anode–Electrolyte Nanointerface. *Nano Lett.* **2021**, *21*, 8220-8228.

15. Hou, S.; Ji, X.; Gaskell, K.; Wang, P.-f.; Wang, L.; Xu, J.; Sun, R.; Borodin, O.; Wang, C. Solvation sheath reorganization enables divalent metal batteries with fast interfacial charge transfer kinetics. *Science* **2021**, *374*, 172-178.

16. Sun, Y.; Zou, Q.; Wang, W.; Lu, Y.-C. Non-passivating Anion Adsorption Enables Reversible Magnesium Redox in Simple Non-nucleophilic Electrolytes. *ACS Energy Lett.* **2021**, *6*, 3607-3613.

17. Eaves-Rathert, J.; Moyer, K.; Zohair, M.; Pint, C. L. Kinetic- versus Diffusion-Driven Three-Dimensional Growth in Magnesium Metal Battery Anodes. *Joule* **2020**, *4*, 1324-1336.

18. Davidson, R.; Verma, A.; Santos, D.; Hao, F.; Fincher, C.; Xiang, S.; Van Buskirk, J.; Xie, K.; Pharr, M.; Mukherjee, P. P.; Banerjee, S. Formation of Magnesium Dendrites during Electrodeposition. *ACS Energy Lett.* **2018**, *4*, 375-376.

19. Aurbach, D.; Lu, Z.; Schechter, A.; Gofer, Y.; Gizbar, H.; Turgeman, R.; Cohen, Y.; Moshkovich, M.; Levi, E. Prototype systems for rechargeable magnesium batteries. *Nature* **2000**, *407*, 724-727.

20. Matsui, M. Study on electrochemically deposited Mg metal. *J. Power Sources* **2011**, *196*, 7048-7055.

21. Aurbach, D.; Cohen, Y.; Moshkovich, M. The Study of Reversible Magnesium Deposition by In Situ Scanning Tunneling Microscopy. *Electrochem. Solid-State Lett.* **2001**, *4*, A113.

22. Jäckle, M.; Helmbrecht, K.; Smits, M.; Stottmeister, D.; Groß, A. Self-diffusion barriers: possible descriptors for dendrite growth in batteries? *Energy Environ. Sci.* **2018**, *11*, 3400-3407.

23. Davidson, R.; Verma, A.; Santos, D.; Hao, F.; Fincher, C. D.; Zhao, D.; Attari, V.; Schofield, P.; Van Buskirk, J.; Fraticelli-Cartagena, A.; Alivio, T. E. G.; Arroyave, R.; Xie, K.; Pharr, M.; Mukherjee, P. P.; Banerjee, S. Mapping mechanisms and growth regimes of magnesium electrodeposition at high current densities. *Mater. Horiz.* **2020**, *7*, 843-854.

24. Wei, C.; Tan, L.; Zhang, Y.; Xi, B.; Xiong, S.; Feng, J.; Qian, Y. Highly reversible Mg metal anodes enabled by interfacial liquid metal engineering for high-energy Mg-S batteries. *Energy Storage Mater.* **2022**, *48*, 447-457.

25. Choudhury, S.; Tu, Z.; Stalin, S.; Vu, D.; Fawole, K.; Gunceler, D.; Sundararaman, R.; Archer, L. A. Electroless Formation of Hybrid Lithium Anodes for Fast Interfacial Ion Transport. *Angew.*

Chem. Int. Ed. **2017**, *56*, 13070-13077.

26. Xiao, P.; Li, H.; Fu, J.; Zeng, C.; Zhao, Y.; Zhai, T.; Li, H. An anticorrosive zinc metal anode with ultra-long cycle life over one year. *Energy Environ. Sci.* **2022**, *15*, 1638-1646.

27. Wang, L.; Snihirova, D.; Deng, M.; Wang, C.; Höche, D.; Lamaka, S. V.; Zheludkevich, M. L. Indium chloride as an electrolyte additive for primary aqueous Mg batteries. *Electrochim. Acta* **2021**, *373*, 137916.

28. Zhao, Y.; Du, A.; Dong, S.; Jiang, F.; Guo, Z.; Ge, X.; Qu, X.; Zhou, X.; Cui, G. A Bismuth-Based Protective Layer for Magnesium Metal Anode in Noncorrosive Electrolytes. *ACS Energy Lett.* **2021**, *6*, 2594-2601.

29. Zhang, J.; Guan, X.; Lv, R.; Wang, D.; Liu, P.; Luo, J. Rechargeable Mg metal batteries enabled by a protection layer formed in vivo. *Energy Storage Mater.* **2020**, *26*, 408-413.

30. Nguyen, D.-T.; Eng, A. Y. S.; Ng, M.-F.; Kumar, V.; Sofer, Z.; Handoko, A. D.; Subramanian, G. S.; Seh, Z. W. A High-Performance Magnesium Triflate-based Electrolyte for Rechargeable Magnesium Batteries. *Cell Rep. Phy. Sci.* **2020**, *1*, 100265.

31. Liang, X.; Pang, Q.; Kochetkov, I. R.; Sempere, M. S.; Huang, H.; Sun, X.; Nazar, L. F. A facile surface chemistry route to a stabilized lithium metal anode. *Nat. Energy* **2017**, *2*, 17119.

32. Hu, K.; Guan, X.; Lv, R.; Li, G.; Hu, Z.; Ren, L.; Wang, A.; Liu, X.; Luo, J. Stabilizing zinc metal anodes by artificial solid electrolyte interphase through a surface ion-exchanging strategy. *Chem. Eng. J.* **2020**, *396*, 125363.

33. Tu, Z.; Choudhury, S.; Zachman, M. J.; Wei, S.; Zhang, K.; Kourkoutis, L. F.; Archer, L. A. Fast ion transport at solid–solid interfaces in hybrid battery anodes. *Nat. Energy* **2018**, *3*, 310-316.

34. Ouyang, K.; Ma, D.; Zhao, N.; Wang, Y.; Yang, M.; Mi, H.; Sun, L.; He, C.; Zhang, P. A New Insight into Ultrastable Zn Metal Batteries Enabled by In Situ Built Multifunctional Metallic Interphase. *Adv. Funct. Mater.* **2021**, *32*, 2109749.

35. Bonnick, P.; Muldoon, J. A Trip to Oz and a Peak Behind the Curtain of Magnesium Batteries. *Adv. Funct. Mater.* **2020**, *30*, 1910510.

36. Mohtadi, R.; Tutusaus, O.; Arthur, T. S.; Zhao-Karger, Z.; Fichtner, M. The metamorphosis of rechargeable magnesium batteries. *Joule* **2021**, *5*, 581-617.

37. Horia, R.; Nguyen, D.-T.; Eng, A. Y. S.; Seh, Z. W. Comparative Study of Conventional Electrolytes for Rechargeable Magnesium Batteries. *Batteries & Supercaps* **2022**, *5*, e202200011.

38. Yoo, H. D.; Liang, Y.; Dong, H.; Lin, J.; Wang, H.; Liu, Y.; Ma, L.; Wu, T.; Li, Y.; Ru, Q.; Jing, Y.; An, Q.; Zhou, W.; Guo, J.; Lu, J.; Pantelides, S. T.; Qian, X.; Yao, Y. Fast kinetics of magnesium monochloride cations in interlayer-expanded titanium disulfide for magnesium rechargeable batteries. *Nat. Commun.* **2017**, *8*, 339.

39. Yu, Y.; Huang, G.; Wang, J. Z.; Li, K.; Ma, J. L.; Zhang, X. B. In Situ Designing a Gradient Li^+ Capture and Quasi-Spontaneous Diffusion Anode Protection Layer toward Long-Life $Li-O_2$ Batteries. *Adv. Mater.* **2020**, *32*, e2004157.

40. Li, Y.; Yang, G.; Sun, S.; Zhang, C.; Lim, C. Y. J.; Wong, A. J. Y.; Lieu, W. Y.; Sofer, Z.; Ng, M.-F.; Liu, W.; Seh, Z. W. High Utilization of Composite Magnesium Metal Anodes Enabled by a Magnesiophilic Coating. *Nano Lett.* **2022**, *22*, 6808-6815.

41. Biswal, P.; Kludze, A.; Rodrigues, J.; Deng, Y.; Moon, T.; Stalin, S.; Zhao, Q.; Yin, J.; Kourkoutis, L. F.; Archer, L. A. The early-stage growth and reversibility of Li electrodeposition in

Br-rich electrolytes. *Proc. Natl. Acad. Sci.* **2021**, *118*, e2012071118.

42. Nguyen, D.-T.; Eng, A. Y. S.; Horia, R.; Sofer, Z.; Handoko, A. D.; Ng, M.-F.; Seh, Z. W. Rechargeable magnesium batteries enabled by conventional electrolytes with multifunctional organic chloride additives. *Energy Storage Mater.* **2022**, *45*, 1120-1132.

43. Zhang, Y.; Li, J.; Zhao, W.; Dou, H.; Zhao, X.; Liu, Y.; Zhang, B.; Yang, X. Defect-Free Metal-Organic Framework Membrane for Precise Ion/Solvent Separation toward Highly Stable Magnesium Metal Anode. *Adv. Mater.* **2022**, *34*, e2108114.

44. Lv, R.; Guan, X.; Zhang, J.; Xia, Y.; Luo, J. Enabling Mg metal anodes rechargeable in conventional electrolytes by fast ionic transport interphase. *Natl. Sci. Rev.* **2020**, *7*, 333-341.

45. Guo, F.; Wu, C.; Chen, S.; Ai, X.; Zhong, F.; Yang, H.; Qian, J. Flaky and Dense Lithium Deposition Enabled by a Nanoporous Copper Surface Layer on Lithium Metal Anode. *ACS Mater. Lett.* **2020**, *2*, 358-366.

46. Xiao, J.; Zhang, X.; Fan, H.; Zhao, Y.; Su, Y.; Liu, H.; Li, X.; Su, Y.; Yuan, H.; Pan, T.; Lin, Q.; Pan, L.; Zhang, Y. Stable Solid Electrolyte Interphase In Situ Formed on Magnesium-Metal Anode by using a Perfluorinated Alkoxide-Based All-Magnesium Salt Electrolyte. *Adv. Mater.* **2022**, *34*, 2203783.

Table of Content (ToC) Graphic